Surfaces and Interfaces 29 (2022) 101796

Contents lists available at ScienceDirect

Surfaces and Interfaces

journal homepage: www.sciencedirect.com/journal/surfaces-and-interfaces

Investigating MCM-41/metal-organic framework nanocomposites as silicon-containing electrodes for supercapacitor

Farshad BoorboorAjdari [a,*], Mohammad Izadpanah Ostad [b], Mahdi Niknam Shahrak [b,*], Mahshid Ershadi [c], Shaghayegh Sadeghi Malek [d], Fatemeh Ghasemi [a], Yalda Zolfaghari [e], Seeram Ramakrishna [f]

[a] Department of Applied Chemistry, Faculty of Chemistry, University of Kashan, Kashan, Iran
[b] Department of Chemical Engineering, Quchan University of Technology, Quchan, Iran
[c] Department of Chemistry, AmirKabir University of Technology, Iran
[d] Pharmaceutical Research Laboratory, Department of Chemistry, Isfahan University of Technology, Isfahan 8415683111, Iran
[e] Faculty of Chemical Engineering, Babol Noshirvani University of Technology, Shariati Ave., Babol 47148-71167, Iran
[f] Department of Mechanical Engineering, Center for Nanofibers and Nanotechnology, National University of Singapore, Singapore

ARTICLE INFO

Keywords:
Supercapacitor
MCM-41
MOF
nanocomposite
Nyquist plots, Silicon

ABSTRACT

For both batteries and supercapacitors, developing electrodes based on Silicon is of enormous interest. The purpose of this study was to prepare two nanocomposites, MZ8 (MCM-41/ZIF-8) and MU66 (MCM-41/UiO-66), that have been specifically designed to function as electrode materials. The cyclic voltammograms showed enlarged potential window and galvanostatic charge-discharge by confirming the samples' successful synthesis process and morphological structure via XRD, FT-IR, TGA, BET, TEM, and FESEM plots gave excellent specific capacitance.

MU66 with spherical morphology and average particle size around 50 nm creates more appropriate pores, and more accessible pathways showed higher capacitance (992 F g^{-1} @ 0.5 Ag^{-1}), while MZ8 (351 F g^{-1} @ 0.5 Ag^{-1}) with hexagonal morphology and average particle size around 350 nm stands more durable (100%) after 4000 cycles. MZ8 displayed an EDLC with semi-rectangular CV and symmetric charge-discharge graphs, while MU66 showed inflation at lower sweep rates and lowered current densities, representing a hybrid charge mechanism. Based on the EIS test, MZ8 showed lower charge resistance and was more conducive to taking the barriers of the low capacitance of Si-based electrodes. We believe that the fabrication of Si-containing materials into MOFs can protect Si from swelling-shrinking and maintain close contact between Si and electrolyte to use both merits of MOF structures and Si capacity.

1. Introduction

As society and the economic progress, it is critical to investigate new and clean energy sources. Supercapacitors (SCs) and lithium-ion batteries (LIBs), which were created as electrochemical energy storage devices, have recently emerged as virtual devices [1–4]. To overcome the low power density and short cycling life of LIBs and the energy density limitations of SCs, promising the materials' electroactivity is a critical step [5–8]. Despite the vital need for novel active electrodes with increased capacities and a longer life span [9–11].

Supercapacitors are energy storage devices with a high power density, a long operational life, a high-rate capability, and a wide operating temperature range. Due to the charge storage mechanism, electrode materials used in supercapacitor applications must have high electrical conductivity, wide accessible surface area, and tailored pore size [12–15].

Two major categories of materials have been used in supercapacitor applications. The first category comprises carbonaceous materials such as carbon fibers, mesoporous carbons, carbon nanotubes, graphene that primarily store charges via non-faradaic double-layer charge storage (EDLC) behavior. The second class of supercapacitor materials consists of transition-metal hydroxides/oxides (such as conductive polymers, $Co(OH)_2$, CeO_2, MnO_2, NiO, and RuO_2). They store charge via redox reactions occurring at the electrode materials' surfaces, commonly known

* Corresponding authors.
E-mail addresses: farshadborbor.2009@gmail.com (F. BoorboorAjdari), m.niknam.sh@qiet.ac.ir (M. Niknam Shahrak).

https://doi.org/10.1016/j.surfin.2022.101796
Received 2 December 2021; Received in revised form 24 January 2022; Accepted 12 February 2022
Available online 13 February 2022

as pseudocapacitors [16–20].

It is critical to create new electrode materials, particularly nanostructured materials with outstanding rate capability and charge storage. It undoubtedly contributes to improving the performance of supercapacitors. Among the various electrode materials, metal-organic frameworks (MOFs) are a novel family of porous materials formed by the chemical reaction of organic linkers with metal ions or clusters [21–23]. MOFs have garnered considerable attention over the last two decades due to their fascinating features like excellent persistent porosity and high surface area, organized crystalline structures, and variable pore diameters [24–26]. Zeolitic imidazolate framework (ZIF) and UiO (Universitetet i Oslo) structures have gained much attention due to the high thermal and chemical stability among different MOFs. UiO-66 consists of 12-connected $[Zr_6O_4(OH)_4]$ clusters with 1,4-benzodicarboxylic acid ligand, while ZIF-8 is made up of zinc ions coordinated by four 2-methylimidazole linkers like Si and Al atoms connected by bridging oxygen atoms in zeolites.

Additionally, MOFs have been used for drug delivery, chemical separations, fluorescence, catalysis, and energy storage [27–30]. Due to the redox behavior of central metal cations and the increased charge transfer within the MOF structure, these nanostructures have been successfully used as electrode materials in energy storage devices. Batteries and supercapacitors are among the recently developed areas [31–33]. However, the as-pioneered MOF-based electrodes still have inappropriate potentials for fulfilling the energy/power-desired demands since they suffer from undesired Coulombic efficiency, low cycle stability, and limited capacity.

Silicon is a promising electrode material for LIBs and SCs due to its high theoretical capacity; nevertheless, Si has the disadvantage of a significant volume change and rapid capacity fading during continuous cycling [34–36]. One of the most common Si-based materials is MCM-41 (stands for Mobil Composition of Matter No. 41), with cylindrical pores making a mesoporous material with a hierarchical structure. The surface modification, characteristics, synthesis, and electrochemical features of efficient electroactive Si-based electrodes are fundamentally addressed. As a result, numerous Si-based electrode morphologies have been created, including Si nanoparticles, Si-doped materials, Si nanowire, Si three-dimensional structure, and Si nano-substrates [37–41]. Thus, it is critical to prevent Si from swelling-shrinking and maintain close contact between Si and its electrolyte and conductive species [42,43].

While research groups have made significant advances to this sector by fabricating various types of Si nanostructures [44] and covering Si surfaces with carbon [45] or metal [46], mass manufacturing is limited due to the method's complexity and cost. By incorporating Si nanostructures into a carbon matrix formed from MOF, the composite's performance would be increased. Due to the matrix's intrinsic open channels, ions are transported more quickly and at a higher rate [47,48]. By incorporating uniformly dispersed metal centers within the porous carbon structure, conductivity and storage capacity are further boosted. A MOF matrix combined with Si nanoparticles can considerably reduce Si's volume change, resulting in extremely high capacity.

Numerous MOF-based compounds have been employed to increase supercapacitor performance, such as Co–Zn/MOF [49], Ni-Co MOF [50], Co–Mn MOF [51], MOF-derived Co_3O_4–C/$Ni_2P_2O_7$ [52], Ni−Co−P/PO_x/C nanosheets [53], Cu-MOF/rGO [54], MOF-Derived CoS_2@CNTs [55]. Also, MCM-41 and its derivatives have shown high potential for supercapacitors, such as, template-assisted (MCM-41) mesoporous Co_3O_4 [56], $Fe_xSn_yMn_{1-x-y}O_2$ deposited on MCM-41 [57], and Fe@MnO_2NPs–MCM-41 [58]. Besides, Feng et al. [59] reported a composite of (PANI)/graphene/(MCM-41), with different contents of graphene oxide and porous silica MCM-41, indicated good capacity (405 F g^{-1}@ 0.8 A g^{-1}) and satisfying capacitance reservation within (91.4%) within 1000 cycles. Prakash et al. [56] worked on MCM-41-template assisted of M41/m-Co_3O_4 nanobuds as an electrode, with exhibition capacity of 228.87 F g^{-1} and retained capacity of 87.5% (@1000 periods).

Here, we worked on preparing two nanocomposites using incorporation between MCM-41 with ZIF-8 and UiO-66 named as MZ8 (MCM-41/ZIF-8) and MU66 (MCM-41/UiO-66), respectively. Then, these two nanocomposites were employed as a silicone-containing electrode in a three-electrode system. According to the electrochemical results, these two substances illustrated the coexistence of typical EDLC and faradaic battery-type behavior. Based on the issues mentioned earlier, the as-designed materials are assumed to protect Si in their frameworks against deforming and assist ion migration by providing proper cavities and channels during charge-discharge cycles. It clearly shows different silicon derivatives inserted in the electrode structure, benefiting higher electrochemical performance and novel electrode design. The MU66 showed higher specific capacity between two MCM-containing MOFs, while MZ8 owned better cycle stability over 4000 cycles.

2. Experimental section

2.1. Materials and reagents

Chemical materials and reagents for the current study including Zn $(NO_3)_2$•$6H_2O$, 2-methylimidazole (Hmim), Ammonium hydroxide solution (25 wt% in water), ethyl alcohol (99%), methyl alcohol (99%), Zirconium (IV) chloride, Terephthalic acid, and Dimethylformamide (DMF) were purchased from Sigma-Aldrich and Merck companies and were utilized purely without any additional treatment.

2.2. Characterization and instruments

Powder X-ray diffraction (XRD) patterns were recorded using Bruker D8-Advance X-ray diffractometer with Cu-Kα (λ=1.54178A°) radiation. Textural characterization of each sample like surface area, pore volume, and pore size distribution was determined from N_2 adsorption-desorption isotherms at 77 K using Micrometrics ASAP 2020 adsorption instrument. The average particle size and surface morphology of each sample was investigated by field emission scanning electron microscopy (FESEM) and Transmission electron microscopy (TEM) analyses taken by TESCAN electron microscope (Mira III, Czech Republic) and Leo 912 AB Omega apparatuses, respectively. Thermo-gravimetric differential scanning calorimetry analysis (TGA-DSC) of the samples was implemented using by Perkin Elmer, Pyris with a heating rate of 10 °C/min. Finally, Fourier-transform infrared (FTIR) spectroscopy was recorded on a Thermo Nicolet Avatar 360 (U.S.A) at room temperature using compacted KBr pellets.

2.3. Electrode preparation and calculating capacity

Here is what was used to prepare the electrode: The active material (80wt%), polyvinylidene difluoride (PVDF, 5wt%) acetylene black (15wt%) were dissolved in N-methyl-2-pyrrolidone (NMP, 10 ml). An electrode was then prepared by spraying a piece of the mixture (10 μL: 0.5 mg) onto a 1 × 1 cm^2 graphite paper and then dried in an oven for 1 hour (3 mg).

To analyze the electrochemical activity of the as-synthesized samples, electrochemical measurements, including cyclic voltammetry (CV), gravimetric charge-discharge (GCD), and electrochemical impedance spectroscopy (EIS) were individually performed in the condition mentioned above. Using the CV and GCD plots in the potential range of −0.9 to 0.1 V ($\Delta V = 1$), the capacitive performance parameters of the samples in the three-electrode system were determined in specific capacitance power density, and energy density [60–62].

$C_s = \frac{I \times \Delta t}{m \times \Delta \nu}$	I(A): current (@ discharge process), m(g): mass of electroactive material, C_s(F g^{-1}): the specific capacitance, ΔV(V): the potential window (applied potential range), Δt (s): discharge period.
$\Delta Q = C_s \times \Delta \nu$	Q(C): the specific capacitance

(continued on next page)

(*continued*)

$\eta = \frac{t_D}{t_C} \times 100$	t_D (s) t_C (s): the discharging and charging duration, η: the coulombic efficiency.

2.4. Preparing and synthesizing procedures

2.4.1. Preparation of UiO-66

UiO-66 was prepared using reported procedures in literature [63, 64]. The synthesis method begins with the addition of 0.125 g $ZrCl_4$ into 5 mL DMF and 1 mL HCl. Subsequently, the resultant solution was sonicated for 20 min to achieve a homogeneous mixture. Then, the solution of terephthalic acid, including 0.123 g terephthalic acid and 10 mL DMF, slowly dissolved in Zr^{4+} solution and sonicated for another 20 min. And then, the mixture was delivered to a Teflon-lined stainless autoclave (120 mL) to remain at 120 °C (12 h). A two-step washing process with DMF and ethanol was conducted on the UiO-66 precipitate before drying (70 °C, 12 h).

2.4.2. Preparation of MCM-41/UiO-66 (MU66)

To prepare MU66 composite,0.125 g Zirconium (IV) chloride and 3 mL HCl was added into 15 mL DMF and stirred for 30 min. Then 0.01 g MCM-41 was added to the emulsion and sonicated for 20 min. Simultaneously, a terephthalic acid solution was prepared by dispersion terephthalic acid (TPA, 0.123 g) in DMF (30 ml) for 30 min. Then it was added into Zr solution and inserted into the autoclave (120 mL) for further reaction at 140 °C for 12 hr. Resulting solution was twice centrifuged with DMF and ethanol. The obtained product was dried at 70 °C (12 h).

2.4.3. Preparation of ZIF-8

ZIF-8 synthesis was followed based on our previous article [65]. Briefly, after dissolving 1 g of Hmim in 12 mL of ethanol, it was added into Zn^{2+} solution containing 0.8 g $Zn(NO_3)_2.6\ H_2O$, and 15 mL ammonium hydroxide solution and stirred for 24 hr. White sediment ZIF-8 was observed after centrifugation and drying at 70 °C. Finally, the as-synthesized ZIF-8 was added into 30 mL methanol and stirred under reflux at 70 °C for 24 hr.

2.4.4. Preparation of MCM-41/ZIF-8 (MZ8)

Fabrication of MZ8 composite was similar to the MU66 synthesis procedure. Hence, 0.01 g MCM-41 was added into Zn^{2+} solution containing 0.32 g dispersed zinc nitrate in 15 mL ammonium hydroxide and sonicated for 20 min. Then the solution was dissolved into Hmim solution containing 0.4 g 2-methylimidazole and 15 mL ethanol. After stirring for 30 min, the combined solution was heated at 140 °C for 12 hr in 120 mL Teflon-lined stainless autoclave. Then, washing and drying were carried out again (ethanol, 70 °C,12 h). Scheme. 1 shows an illustration of the preparing procedure of electrode materials.

3. Result and discussion

3.1. Characterization of the samples

Powder X-ray diffraction measurements for pure and composite samples are revealed in Fig. 1. As it can be observed, segregated peaks at around 7.28°, 10.24°, 12.74°, and 18.5° in the MZ8 sample confirm the formation and loading of ZIF-8 in MZ8 composite [65,66]. Also appeared peaks at 2θ=7.6°, 8.7°, and 26° indicate the presence of UiO-66 in MU66 composite [67]. Although the XRD patterns of both composites show a slight reduction in the crystallinity of ZIF-8 and UiO-66 owing to the amorphous characteristic of MCM-41, the formation of composites with maintaining the inherent properties of each structure can be approved [68–70].

FTIR analyses of the pure ZIF-8 and UiO-66 and their composites MZ8 and MU66 have been depicted in Fig. 2. According to Fig. 2, for ZIF-8 and MZ8, the appeared peaks at 421, and 1586 cm^{-1} are due to the stretching vibrations of Zn–N and C–N bonds, respectively. Additionally, observed peak values around 759, 1145, and 1308 cm^{-1} are associated with the imidazole ring bending signals. The stretching vibration of the imidazole ring was also measured at 1422 cm^{-1}. C–H stretching vibrations were also observed at 2930 and 3135 cm^{-1} for aromatic and aliphatic C—H, confirming the formation of the ZIF-8 structure [65, 71].

Additionally, the FTIR patterns of UiO-66 and MU66 showed multiple peaks around 1400 cm^{-1} and 1656 cm^{-1}, corresponding to the stretching vibration on C = O. There are peaks at 661 cm^{-1}corresponding to Zr–O stretching bands and at 2930 cm^{-1} corresponding to C–H [72]. Also, extra appeared peaks at around 1050, 1700, 2930, and

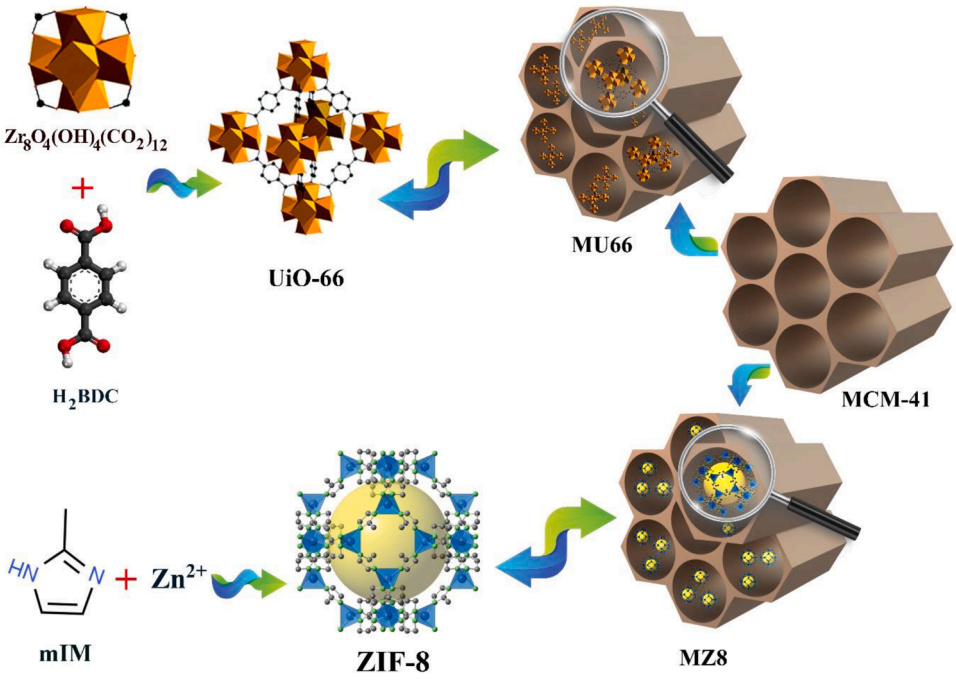

Scheme 1. An illustration of synthesis mechanism.

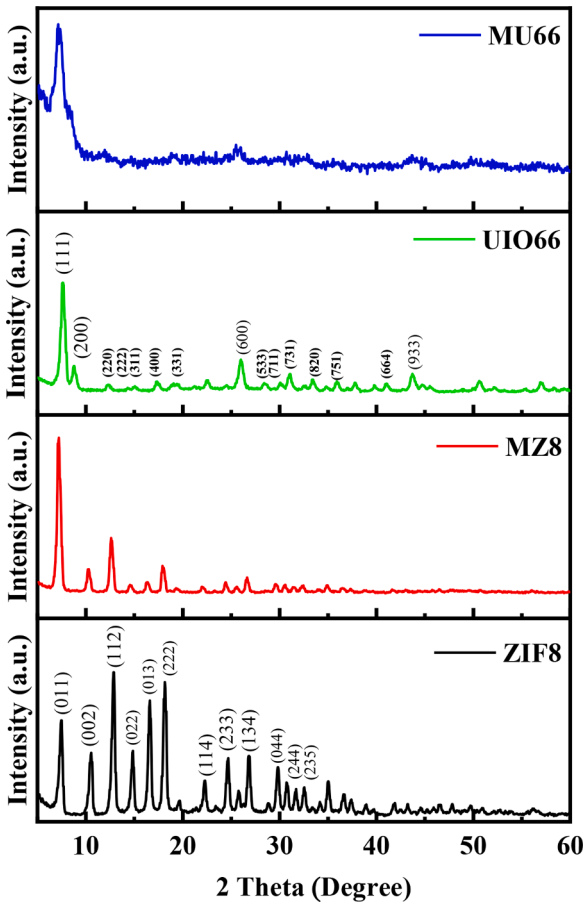

Fig. 1. XRD patterns of ZIF-8, MZ8, UiO-66, and MU66.

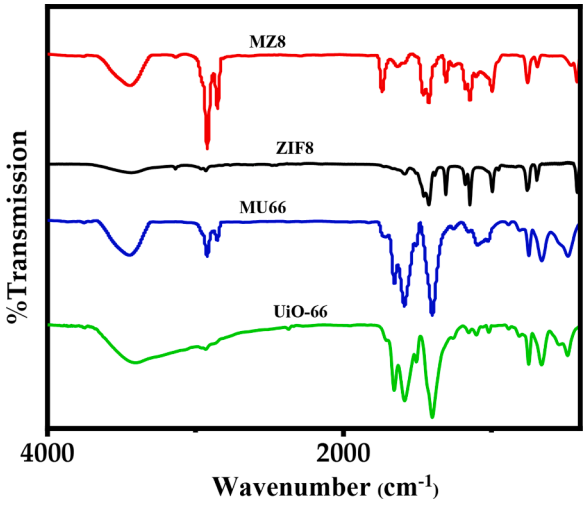

Fig. 2. FTIR patterns of ZIF-8, MZ8, UiO-66, and MU66.

3450 cm^{-1} confirm the presence of Si–O–Si, N–H, OH, and CH_2 vibrations of MCM-41 in the MZ8 and MU66 composites [69,73].

The N_2 adsorption-desorption measurements of the ZIF-8, MZ8, UiO-66, and MU66 samples and MCM-41 structure were performed at 77 K to find the textural properties of nanocomposites compared to pure MOFs (Fig. 3 and Table 1). Moreover, the BJH pore size distribution of all samples is shown in Fig. S1.

The N_2 adsorption-desorption isotherms of MOFs (UiO-66 and ZIF-8) exhibit type IV and type I sorption behavior, illustrating the structures' mesoporosity and microporosity characteristics with average pore size 3.04 and 2.14 nm, respectively. Furthermore, after incorporating MCM-41 with pure ZIF-8 networks, the isotherm of nanocomposite indicated a hysteresis loop around P/P0 = 0.5 with a combined isotherm behavior of type I (sharp increase in N_2 adsorption) and type IV (hysteresis loop). The observed hysteresis loop in the MZ8 affirms the MCM-41 mesopore structure and nanocomposite formation. On the other hand, for MU66 nanocomposite, the type IV behavior of sorption isotherm remains while its hysteresis loop has become wider. According to the reported data in Table 1, both MZ8 and MU66 nanocomposites have shown an enhancement in N_2 amount of adsorption (BET surface area) compared to MCM, suggesting the formation of ZIF-8 and UiO-66 inside the channels of MCM-41.

Interestingly, the increase in surface area of MZ8 nanocomposite is much larger than that observed for MU66. It is derived from the microporosity feature of ZIF-8. While the BET surface area of MCM-41 is measured at around 224 $m^2\ g^{-1}$, MZ8 and MU66 nanocomposites indicate a BET surface area equal to 1575 and 254 $m^2\ g^{-1}$, respectively. Table 1 illustrates a reduction in the pore volume of MCM-41 in MU66 and MZ8 samples from 1 to 0.49 and 0.76 cc/g. It is evidenced by the presence of MOFs inside the channels of MCM-41 [69].

FESEM and TEM images and histograms of the particle size distribution of pristine MOFs and their nanocomposites are demonstrated in Fig. 4, Fig. 5, and Fig. S2, respectively. According to FESEM images (Fig. 4a and c) and particle size distribution (Fig. S2), ZIF-8 and UiO-66 particles reveal relatively uniform hexagonal and semi-spherical shapes with average particle sizes around 350 and 50 nm, respectively. After hybridizing ZIF-8 and UiO-66 with MCM-41, the SEM image of MZ8 nanocomposite (Fig. 4b) shows some hexagonal particles of ZIF-8 alongside spherical particles MCM-41. This observation indicates that in the prepared MZ8, besides the formation of most ZIF-8 inside the MCM-41 structure, some MOF particles are formed on the outside surface of MCM-41 [49]. Nonetheless, the SEM image of MU66 (Fig. 4d) exhibits only spherical particles related to MCM. Furthermore, the TEM image of MZ8 (Fig. 5b) unveils relatively similar that of the image for ZIF-8 (Fig. 5a) because of the partial coverage of MCM-41 by ZIF-8 particles, while from the TEM image of MU66 (Fig. 5d), the presence of UiO-66 particles inside the MCM structure is evident.

In Fig. 6, the thermal stability of ZIF-8, MZ8, UiO-66, and MU66 are compared by TGA analysis. Thermogravimetric analysis of ZIF-8 and MZ8 shows that these materials decomposed around 450 °C and 600 °C, respectively. Also, for UiO-66 and MU66 samples, thermal decompositions fall out 450 °C and 550 °C, respectively. The observed shift in enhancing the thermal stability of nanocomposites is attributed to the presence of MCM-41 in the structures [74,75].

4. Electrode preparation

Three electrode set-up was employed in electrochemical analysis to determine the electrochemical behavior of the MZ8 and MU66 as working electrodes. All components, including counter (platinum wire), reference (Ag/AgCl), and working (MZ8 and MU66) electrodes, were overwhelmed in an alkaline (KOH, 6 M) environment. The active material (80wt%), polyvinylidene difluoride (PVDF, 5wt%) acetylene black (15wt%) were dissolved in N-methyl-2-pyrrolidone (NMP, 10 ml). An electrode was then prepared by spraying a piece of the mixture (10 μL: 0.5 mg) onto a 1 × 1 cm^2 graphite paper and then dried in an oven for 1 hour (3 mg).

4.1. Electrochemical measurements (CVs & GCDs)

Fig. 7 illustrates the cyclic voltammograms and GCDs of the MZ8 and MU66 working electrodes. CV curves for both electrodes were drawn with counting rates ranging from 10 to 400 mV s^{-1} (Fig. 7a, b), which exhibit a quasi-rectangular configuration, implying the coexistence of EDLC and faradaic battery-type activity [76,77]. Figure S3 shows

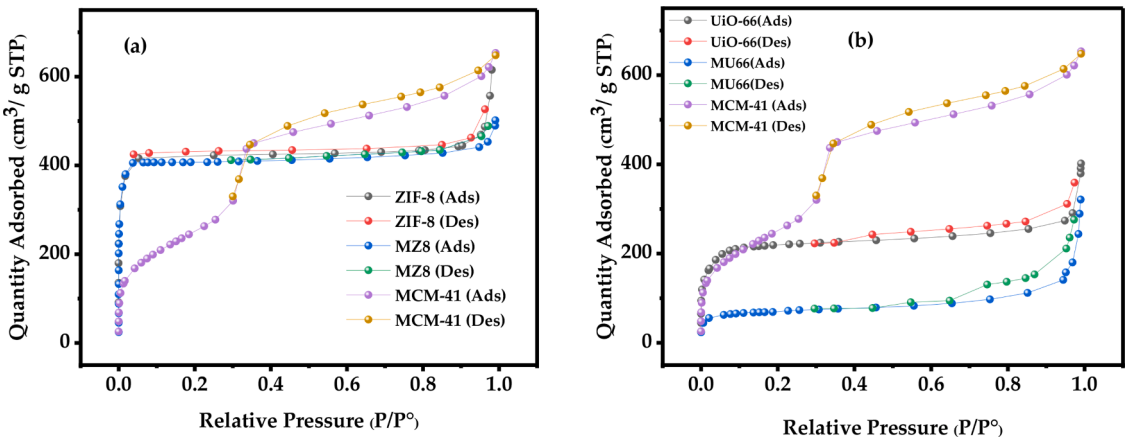

Fig. 3. BET isotherms of a) ZIF-8, MZ8, and MCM-41, b) UiO-66, MU66, and MCM-41.

Table 1
Structural properties of all synthesized samples.

Samples	S_{BET} (m^2 g^{-1})	Total pore volume ($cm^3 g^{-1}$)	Mean pore diameter (nm)
ZIF-8	1771	0.95	2.14
MZ8	1575	0.76	1.93
UiO-66	799	0.60	3.04
MU66	254	0.49	7.81
MCM-41	224	1.00	4.16

three-dimensional (3D) CCVs of MZ8 and MU66 electrodes, which was performed during 4000 cycles at the scan rate of 400 mV s^{-1}. In these 3D plots, the changes in the CVs over cycle number are more noticeable and it's evident that CV curves keep their initial shape even after these cycles. Compared to the MZ8, the MU66 electrode has a wider CV area, resulting in a higher specific capacitance (Fig. 7c). Both samples' GCD plots (Fig. 8a) were compared (at 1 A g^{-1}) and then plotted independently at varied current densities of 0.5, 1, 2, 4, and 8 A g^{-1} and then compared at 1 A g^{-1} (Fig. 8b, c). They exhibited a modest divergence from linear behavior, demonstrating the electrode's characteristic

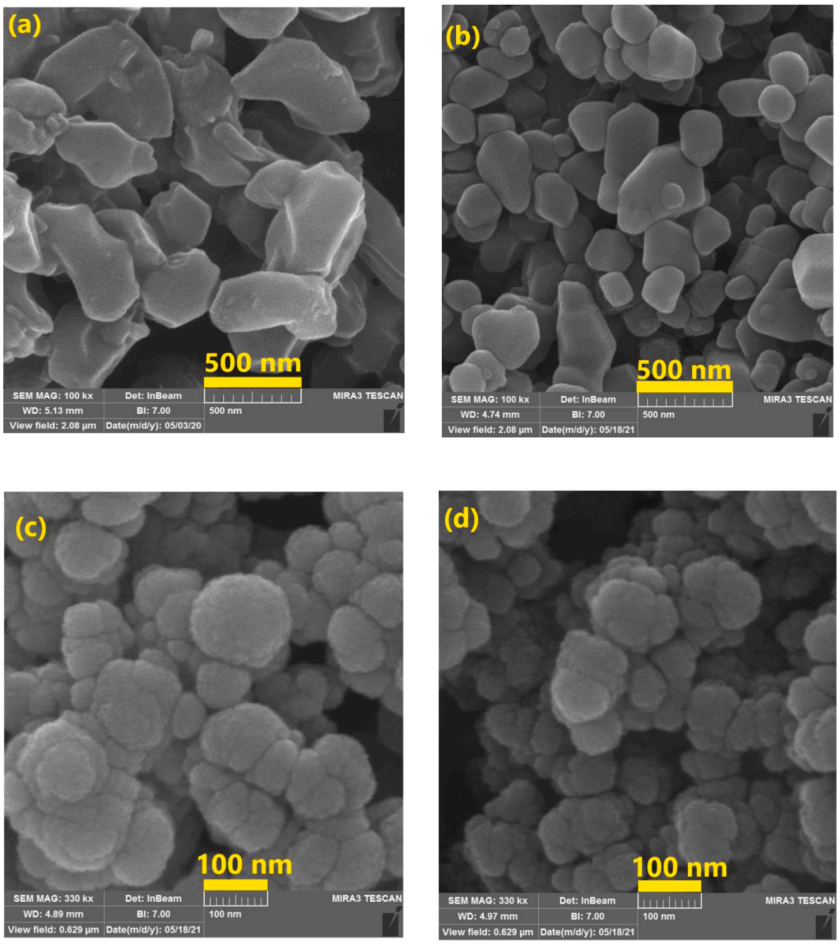

Fig. 4. FESEM of a) ZIF-8, b) MZ8, c) UiO-66 and d) MU66.

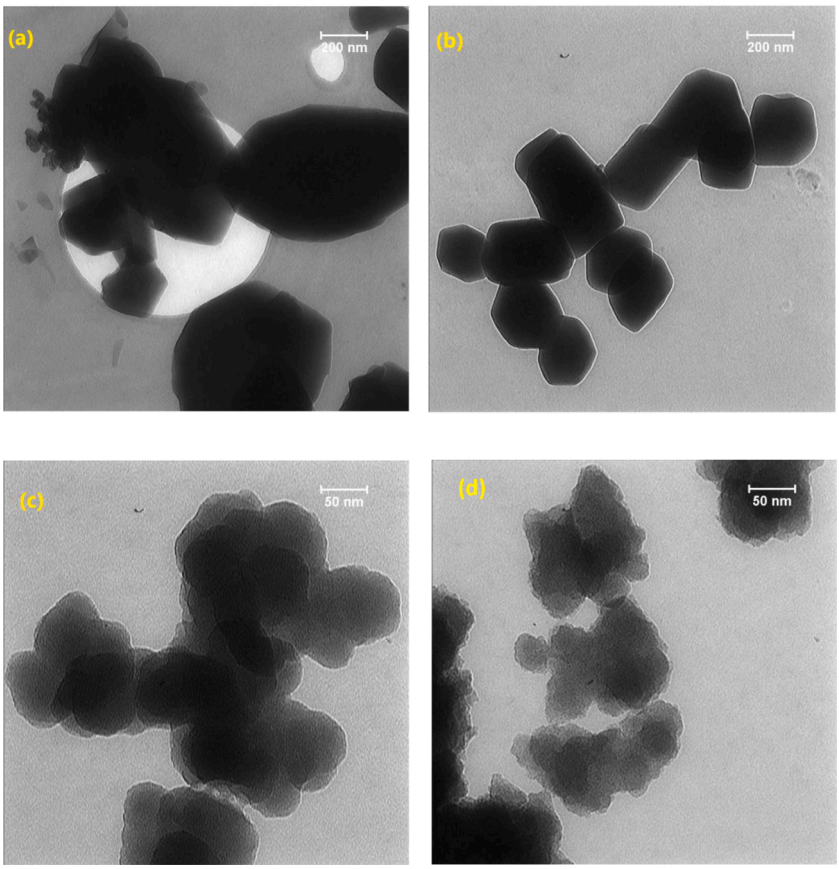

Fig. 5. TEM images of a) ZIF-8, b) MZ8, c) UiO-66 and d) MU66.

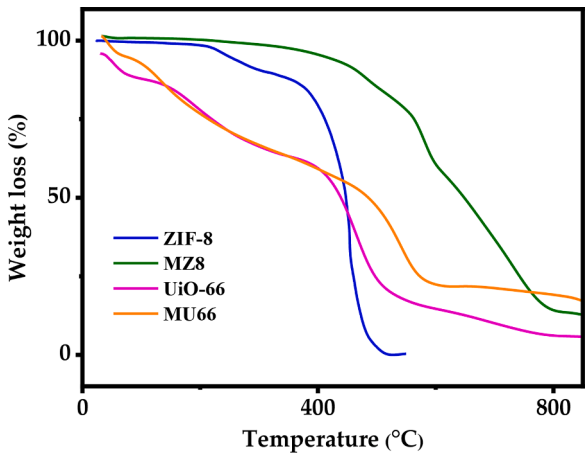

Fig. 6. TGA curves of synthesized samples.

dominating EDLC and faradaic activity to a lesser extent. By increasing the current density rate and scan for MU66, the peaks disappeared in CVs, and inflation was slightly smoothed in GCDs, showing the contribution of simultaneous charge mechanisms. Additionally, a minor bending in low current density can be attributed to the nitrogen in MOF structures or metal-centers and their oxidation in alkaline media or to the surface faradaic reaction that happens in the presence of the electrolyte.

A significant shortcoming of silicon-based electrodes is their low capacity and rapidly declining efficiency. For instance, Kumar et al. [78] worked on the microstructure of the silicon particles in three-electrode system with 80% retention capacity. It may be resulted from the instability and volume expansion of silicone particles. Also, the porosity and effective channels are necessary for delivering ions and diffusion process. The chip-based etching technique for silicon Silicon produces a structure with a strong mechanical contact between the active silicon material and the doped silicon collector material to integrate into applications.

Mechanically integrated devices with tunable porosity, thickness, and shape may be incorporated into existing silicon-based technological platforms to provide effective energy storage. Graphene-coating, metal oxides, and conductive polymers were interestingly used with Silicon in SCs [78–81]. The porous and tuned structure of as-designed MCM-41/ZIF-8 and MCM-41/UiO-66 improves not only electrolyte penetration/diffusion and the MOF framework efficiently limits the electrolyte penetration/diffusion expansion difficulties and provides increased structural stability throughout continuous cycles.

The specific capacitances of the MZ8 and MU66 samples were determined in response to sweeping rates (Fig. S4-a, b) and current densities (Fig. S4-c, d). Increased sweep rates resulted in a steady decline in a specific capacity.

While big pores facilitate electrolyte transport, microscopic pores maximize the electrochemical surface area accessible for reactions. The large surface area results from these microscopic holes [82–84]. Slower sweep rates allow more K^+ or H^+ ions to penetrate holes in electrode surfaces and channels, increasing the number of accessible surface or active sites for redox processes. However, their capacities are dramatically reduced at higher scan rates due to occupied active sites that prevent ions from bonding with the electrode material's surface. MZ8 and MU66 electrodes had specific capacitances of 351 and 992 F g^{-1} at 0.5 A g^{-1}, and 110 and 286 F g^{-1} at 1 A g^{-1}, respectively (Fig. S4-c, and S4-d).

MZ8 has a lower capacitance while having the most significant surface area. Because only a portion of the pores is successfully employed

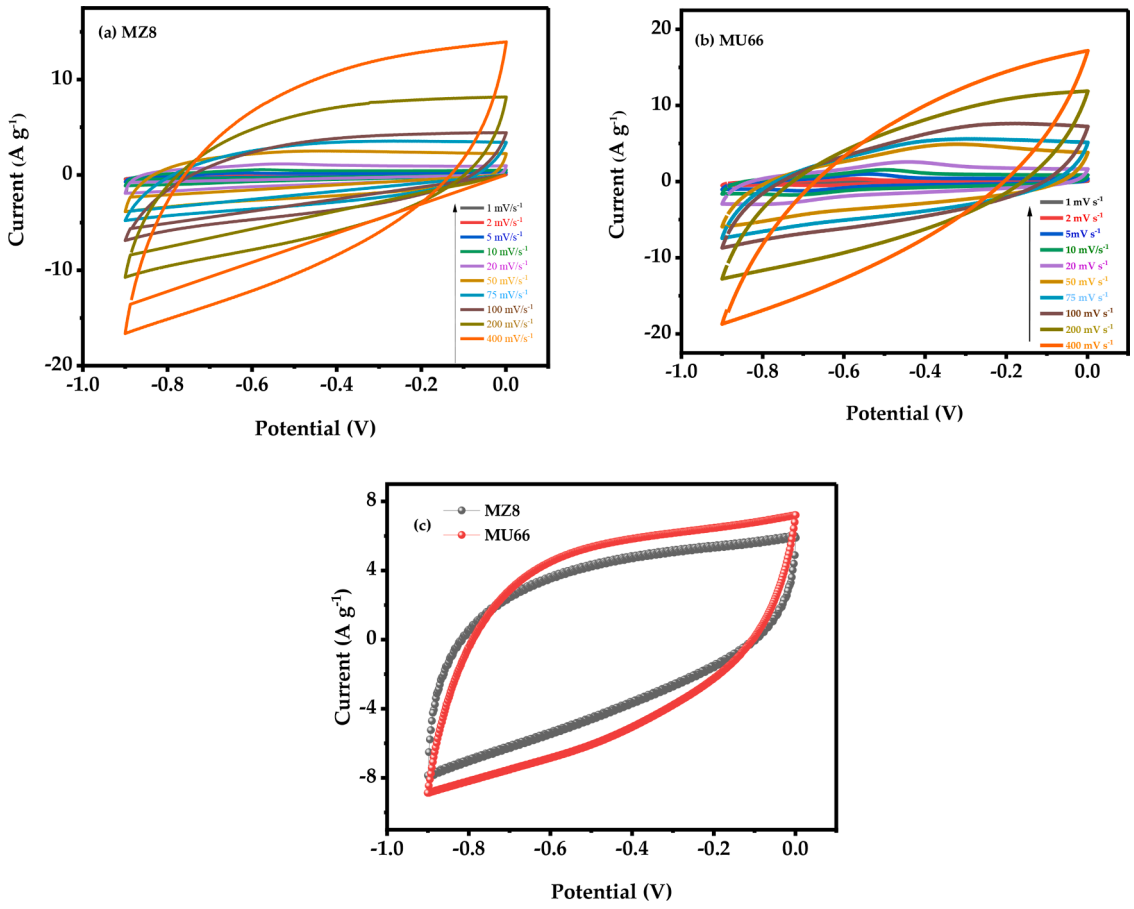

Fig. 7. Cyclic voltammetry at different scan rate (10–400 mV s^{-1}) for (a) MZ8, and (b) MU66. (c) Comparison of CV diagrams for MZ8and MU66.

for charge transfer, the surface area is less important than the specific surface area. Previously published literature validated this observation, reaching a similar result [85–87]. While MU66 has the smallest specific area, the increased capacity can be attributed to more accessible active sites and sufficient ion diffusion channels, advantageous for super-capacitors' effective electrochemical charge storage mechanism. At lower sweep rates and current densities, there are plentiful and highly accessible active sites combined with physically adsorbed redox-active contents on the electrode surfaces, resulting in suitable capacitance, particularly for MU66. The specific capacitances rapidly decreased due to the occupation of the MOF-adjusted pore size and a lack of active sites in the electrodes.

A considerable percentage of the rapid capacity degradation of Si-based electrodes is due to structural instability, in which significant volumetric changes in Silicon (>300%) significantly reduce the mechanical stability of electrodes, hence restricting their electrochemical performance [88]. Additionally, poor electronic conductivity affects the rate of electrochemical reactions, reducing Si's participation [89,90]. As a result, the MZ8 and MU66 samples have been designed to address those issues by forming a hybrid structure that facilitates electron/ion migration and increases the structural stability of Si-based materials.

Both MZ8 and MU66 demonstrated exceptional stability, with MU66 exhibiting roughly 2% capacity loss and MZ8 retaining 100% of initial capacity after 4000 consecutive charge/discharge cycles (Fig. S5). It indicates that the chemical or physical structures of the as-synthesized electrodes are likely to be quite durable throughout charge/discharge cycles. Whereas Feng et al. recently synthesized polyaniline / MCM-41 / graphene through a hydrothermal process and investigated its electrochemical performance in a three-electrode system, where after 1000 cycles, the specific capacitance of the composite reached to 91.4% of its initial value [59].

It is also argued that the coexistence of the central metals in the ZIF-8 and UiO-66 and with imidazole framework can also contribute to MCM (silicon abundance) working. The presence of Cobalt and Zirconium may contribute to the high initial capacitance, and then MCM/MOF shows a synergistic effect, intensified by electrolyte ion diffusion.

Also, Fig. 9 provides information on the frequency response of MZ8 and MU66 in EDLCs, taking into consideration the electrochemical impedance spectra. The Nyquist plots exhibit a semicircle form at higher domains for MZ8 and MU66 samples, corresponding to the charge transfer resistance at the interfacial of electrode/electrolyte (R_{ct}) [91, 92]. The results show that MZ8 has a low resistance at interface contact due to its decorous pore size, facilitating electrolyte ion transport.

When the vertical curve appears at low frequencies, this implies good capacitive behavior and rapid diffusion of electrolytes (OH^- and K^+) in electrode pores [78,93–95], i.e., a steeper slope intimate ideal capacitance behavior. The Warburg resistance could shift the vertical line concerning the electrolyte ions. Compared to MU66, the MZ8 shows the steepest EIS curve, resulting in the slightest Warburg resistance, revealing more desirable conductivity as an electrode material. Although MZ8 nanocomposite showed a more conductive nature than MU66, the proper pore size of MU66 offers more capacitance due to efficient pathways for ion transfer. The measured R_s, R_{ct}, and Z_w are compared in Table 2 for both MZ8 and MU66 samples. Furthermore, Table 3 compares the electrochemical performances of the MZ8, the MU66 with reported electrodes in specific capacitance and retention capacity within different cycles.

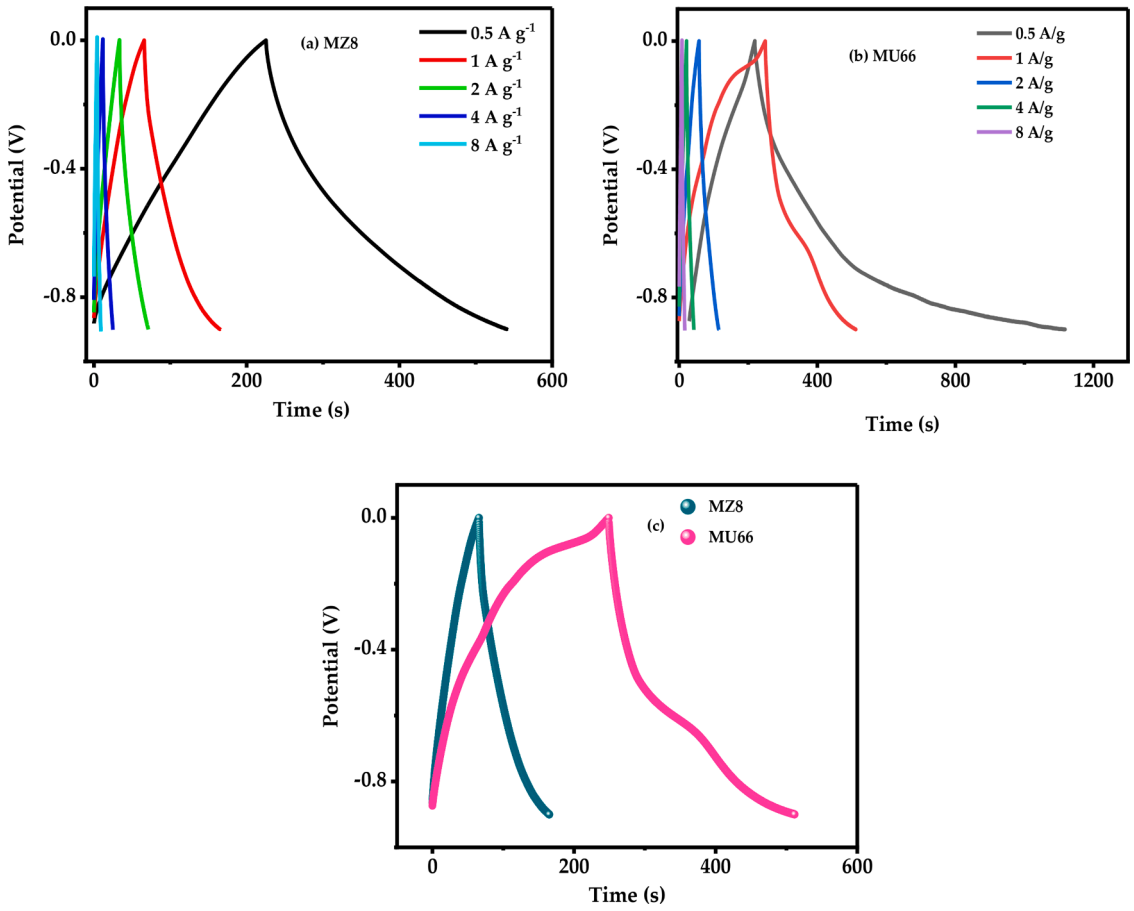

Fig. 8. (c) Comparison of Galvanic charge/discharge at 1A g^{-1}. Galvanic charge/discharge plots (a) MZ8, and (b) MU66.

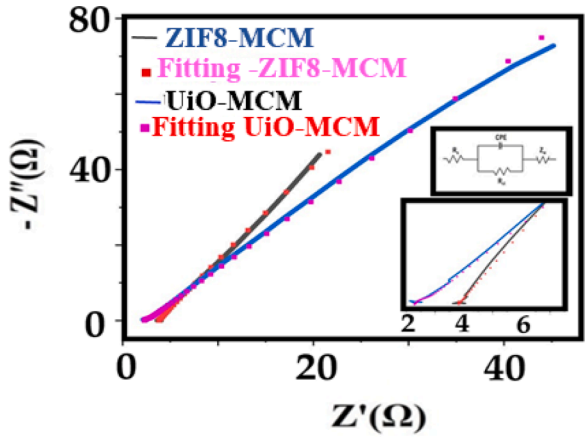

Fig. 9. Impedance spectroscopy for MZ8and MU66.

Table 2
An analysis of EIS results of different electrodes in a three-electrode system.

Electrode	R_S	CPE	R_{ct}	Z_W
MZ8	3.7	0.103	0.341	3.98
MU66	2.24	0.05	0.402	8.1

5. Conclusion

Two MZ8 and MU66 were considered as electrode materials in a three-electrode supercapacitor. The structural characterizations proved the promising approaches of preparing electrodes.

Furthermore, the electrochemical tests were carried out in KOH [6 M] with accessible pathways for ion delivery and electroactive sites. The BET analysis showed more pore diameter for MU66, while MZ8 had the highest surface area. MU66 could efficiently decrease resistance and provide proper K^+ and H^+ diffusion channels based on the EIS measurements. The specific capacitance of MU66 and MZ8 obtained 992 and 351 F g^{-1} at the current density of 0.5 A g^{-1} due to accessible active sites. MZ8 showed an EDLC with semi-rectangular CV and symmetric charge-discharge plots concerning the storing mechanism.

In contrast, MU66 at lower sweep rate and current densities showed inflation, representing hybrid charge storage behavior. MZ8 showed more cycling stability after 4000 continuous charge-discharge processes, where MU66 lost 2% of initial capacity, meaning excellent cycle stability of both electrodes. Inserting Si into MOF frameworks can offer desirable electrochemical outputs, requiring more designing and engineering electrodes.

CRediT authorship contribution statement

Farshad BoorboorAjdari: Conceptualization, Formal analysis, Investigation, Resources, Writing – original draft, Writing – review & editing, Visualization, Supervision. **Mohammad Izadpanah Ostad:** Methodology, Formal analysis, Resources, Software. **Mahdi Niknam Shahrak:** Conceptualization, Formal analysis, Methodology, Investigation, Resources, Writing – original draft, Writing – review & editing, Supervision. **Mahshid Ershadi:** Conceptualization, Methodology, Formal analysis, Resources, Writing – review & editing, Software. **Shaghayegh Sadeghi Malek:** Conceptualization, Resources, Writing – review & editing. **Fatemeh Ghasemi:** Formal analysis, Resources,

Table. 3
The reported Si-based electrodes in different media for supercapacitors.

Electrode	Electrolyte	Specific Capacitance (F g^{-1})	Current density (A g^{-1})	Retention capacity% (Cycles)	Ref.
graphene/PANI/MCM-41 (50% GO content)	KOH [6 M]	405 (F g^{-1})	0.8 (A g^{-1})	91.4% (1000)	[59]
SiPDC-2	KOH [6 M]	251 (F g^{-1})	0.2 (A g^{-1})	94% (2000)	[96]
M41/m-Co_3O_4 nanobud	KOH [1 M]	228.87(F g^{-1})	5 (mV s^{-1})	87.5% (1000)	[56]
RHC (with SiO_2)	KOH [6 M]	40.8 (F g^{-1})	0.1 (A g^{-1})	–	[97]
		21.6 (F g^{-1})	0.3 (A g^{-1})		
C-ZIF-8@MWCNTs		259.2 (F g^{-1})	0.5 (A g^{-1})	92% (5000)	[98]
RHPC (removing SiO_2)	KOH [6 M]	110.2 (F g^{-1})	0.1 (A g^{-1})	78% (5000)	[97]
		100 (F g^{-1})	0.3 (A g^{-1})		
		86 (F g^{-1})	1 (A g^{-1})		
SiOCC-30 (30% SiO_2)	[TEA] [1 M]	41.8 (F g^{-1})	10 (mA g^{-1})	92.1% (10,000)	[99]
Si@C(3)/MnO_2	phosphoric acid [3 M]	240.1(F g^{-1})	1 (A g^{-1})	85.2% (2000)	[100]
PEDOT/PSS-SWNT	$NaNO_3$ [1 M]	104 (F g^{-1})	1 (A g^{-1})	90% (1000)	[101]
rGO/ZIF-67	KOH [6 M]	210 (F g^{-1})	1 (A g^{-1})	80% (1000)	[102]
PPy@UIO-66@CT	H_2SO_4[1 M]	565 (F g^{-1})	0.8 (A g^{-1})	90% (500)	[103]
MWCNT/NPC-L	H_2SO_4[1 M]	302.2 (F g^{-1})	2 (A g^{-1})	95.8% (10,000)	[104]
PANI/UiO-66	H_2SO_4[1 M]	647 (F g^{-1})	1 (A g^{-1})	91% (5000)	[105]
C-ZIF-8@MWCNTs	H_2SO_4[1 M]	326 (F g^{-1})	1 (A g^{-1})	99.7% (10,000)	[106]
MZ8	**KOH, [6 M]**	**351 (F g^{-1})**	**0.5 (A g^{-1})**	**100% (4000)**	**This Work**
		110 (F g^{-1})	**1 (A g^{-1})**		
MU66	**KOH, [6 M]**	**992 (F g^{-1})**	**0.5 (A g^{-1})**	**98% (4000)**	**This Work**
		286(F g^{-1})	**0.5 (A g^{-1})**		

Writing – review & editing, Software. **Yalda Zolfaghari:** Methodology, Formal analysis, Writing – review & editing. **Seeram Ramakrishna:** Conceptualization, Formal analysis, Investigation, Resources, Writing – original draft, Writing – review & editing, Visualization.

Declaration of Competing Interest

The authors declare that they have no known competing financial interests or personal relationships that could have appeared to influence the work reported in this paper.

Supplementary materials

Supplementary material associated with this article can be found, in the online version, at doi:10.1016/j.surfin.2022.101796.

References

[1] T. Zeng, D. Feng, Conductive carbon networks in surface coating of GeP rods toward high-performance lithium/sodium-ion battery anode, Surf. Interf 27 (2021), 101461, https://doi.org/10.1016/j.surfin.2021.101461.

[2] M. Kim, H. Lim, X. Xu, M.S.A. Hossain, J. Na, N.N. Awaludin, J. Shah, L. K. Shrestha, K. Ariga, A.K. Nanjundan, D.J. Martin, J.G. Shapter, Y. Yamauchi, Sorghum biomass-derived porous carbon electrodes for capacitive deionization and energy storage, Microporous Mesoporous Mater 312 (2021), 110757, https://doi.org/10.1016/j.micromeso.2020.110757.

[3] F. Boorboor Ajdari, E. Kowsari, M. Niknam Shahrak, A. Ehsani, Z. Kiaei, H. Torkzaban, M. Ershadi, S. Kholghi Eshkalak, V. Haddadi-Asl, A. Chinnappan, S. Ramakrishna, A review on the field patents and recent developments over the application of metal organic frameworks (MOFs) in supercapacitors, Coord. Chem. Rev. 422 (2020), 213441, https://doi.org/10.1016/j.ccr.2020.213441.

[4] M.S. Mohammadnia, E. Naghian, M. Ghalkhani, F. Nosratzehi, K. Adib, M. M. Zahedi, M.R. Nasrabadi, F. Ahmadi, Fabrication of a new electrochemical sensor based on screen-printed carbon electrode/amine-functionalized graphene oxide-Cu nanoparticles for Rohypnol direct determination in drink sample, J. Electroanal. Chem. 880 (2021), 114764.

[5] X. Jiao, X. Yuan, J. Yin, F. Boorboor Ajdari, Y. Feng, G. Gao, J. Song, Multiple network binders via dual cross-linking for silicon anodes of lithium-ion batteries, ACS Appl. Energy Mater. 4 (2021) 10306–10313.

[6] X. Chen, F. Su, Q. Zhou, J. Sun, High-performance all-solid-state flexible asymmetric supercapacitors composed of PPy@Ti3C2Tx/CC and Ti3C2Tx/CC electrodes, Surfaces and Interfaces 26 (2021), 101393, https://doi.org/10.1016/j.surfin.2021.101393.

[7] A. Xie, H. Wang, Z. Zhu, W. Zhang, X. Li, Q. Wang, S. Luo, Mesoporous CeO2-α-MnO2- reduced graphene oxide composite with ultra-high stability as a novel electrode material for supercapacitor, Surf. Interf 25 (2021), 101177, https://doi.org/10.1016/j.surfin.2021.101177.

[8] K. Asare, M.F. Hasan, A. Shahbazi, L. Zhang, A comparative study of porous and hollow carbon nanofibrous structures from electrospinning for supercapacitor electrode material development, Surf. Interf 26 (2021), 101386, https://doi.org/10.1016/j.surfin.2021.101386.

[9] S. Xiong, S. Jiang, J. Wang, H. Lin, M. Lin, S. Weng, S. Liu, Y. Jiao, Y. Xu, J. Chen, A high-performance hybrid supercapacitor with NiO derived NiO@ Ni-MOF composite electrodes, Electrochim. Acta. 340 (2020), 135956.

[10] L. Zhu, Z. Yao, T. Liu, C. Xu, D. Cai, B. Sa, Q. Chen, H. Zhan, A lightweight and low-cost electrode for lithium-ion batteries derived from paper towel supported MOF arrays, Chem. Commun. 56 (2020) 5847–5850.

[11] C. Gao, Z. Jiang, P. Wang, L.R. Jensen, Y. Zhang, Y. Yue, Optimized assembling of MOF/SnO2/graphene leads to superior anode for lithium ion batteries, Nano Energy 74 (2020), 104868.

[12] H.R. Naderi, A. Sobhani-Nasab, M. Rahimi-Nasrabadi, M.R. Ganjali, Decoration of nitrogen-doped reduced graphene oxide with cobalt tungstate nanoparticles for use in high-performance supercapacitors, Appl. Surf. Sci. 423 (2017) 1025–1034, https://doi.org/10.1016/j.apsusc.2017.06.239.

[13] J. Yin, W. Zhang, N.A. Alhebshi, N. Salah, H.N. Alshareef, Synthesis strategies of porous carbon for supercapacitor applications, Small Methods 4 (2020), 1900853.

[14] S. Begum, R.R. Haikal, A.H. Ibrahim, M.A.E. Safy, M. Tsotsalas, M.H. Alkordi, Flash synthesis for conformal monolithic coatings of the Zr-based metal-organic framework (UiO-66-NH2) on non-modified surfaces: applications in thin-film electrode systems, Surf. Interf 20 (2020), 100587, https://doi.org/10.1016/j.surfin.2020.100587.

[15] X. Yue, R. Hu, D. Zhu, J. Qi, Y. He, Q. Meng, F. Wei, Y. Ren, Y. Sui, Controlled synthesis and formation mechanism of flower-like CuS/NiS microspheres for supercapacitors, Surf. Interf 22 (2021), 100871, https://doi.org/10.1016/j.surfin.2020.100871.

[16] Z. Wang, K. Zhao, S. Lu, W. Xu, Application of flammulina-velutipes-like CeO2/Co3O4/rGO in high-performance asymmetric supercapacitors, Electrochim. Acta. 353 (2020), 136599.

[17] A. Mohanty, D. Jaihindh, Y.-.P. Fu, S.P. Senanayak, L.S. Mende, A. Ramadoss, An extensive review on three dimension architectural metal-organic frameworks towards supercapacitor application, J. Power Sources. 488 (2021), 229444.

[18] M. Rahimi-Nasrabadi, V. Pourmohamadian, M.S. Karimi, H.R. Naderi, M. A. Karimi, K. Didehban, M.R. Ganjali, Assessment of supercapacitive performance of europium tungstate nanoparticles prepared via hydrothermal method, J. Mater. Sci. Mater. Electron. 28 (2017) 12391–12398.

[19] K. Adib, E. Sohouli, M. Ghalkhani, H.R. Naderi, Z. Rezvani, M. Rahimi-Nasrabadi, Sonochemical synthesis of Ag2WO4/RGO-based nanocomposite as a potential material for supercapacitors electrodes, Ceram. Int. 47 (2021) 14075–14086.

[20] A. Khoshroo, L. Hosseinzadeh, K. Adib, M. Rahimi-Nasrabadi, F. Ahmadi, Earlier diagnoses of acute leukemia by a sandwich type of electrochemical aptasensor based on copper sulfide-graphene composite, Anal. Chim. Acta. 1146 (2021) 1–10.

[21] J. Pokharel, A. Gurung, A. Baniya, W. He, K. Chen, R. Pathak, B.S. Lamsal, N. Ghimire, Y. Zhou, MOF-derived hierarchical carbon network as an extremely-high-performance supercapacitor electrode, Electrochim. Acta. 394 (2021), 139058.

[22] L. Lei, X. Zhang, Y. Su, S. Wu, J. Shen, Metal–organic framework (MOF)-assisted construction of core–shell nanoflower-like CuO/CF@ NiCoMn–OH for high-performance supercapacitor, Energy & Fuels 35 (2021) 8387–8395.

[23] A.H. Vahabi, F. Norouzi, E. Sheibani, M. Rahimi-Nasrabadi, Functionalized Zr-UiO-67 metal-organic frameworks: structural landscape and application, Coord. Chem. Rev. 445 (2021), 214050.

[24] M. Ali, E. Pervaiz, T. Noor, O. Rabi, R. Zahra, M. Yang, Recent advancements in MOF-based catalysts for applications in electrochemical and photoelectrochemical water splitting: a review, Int. J. Energy Res. 45 (2021) 1190–1226.

[25] C.T. Lee, M.W. Shin, Solvothermal growth of Mg-MOF-74 films on carboxylic functionalized silicon substrate using acrylic acid, Surf. Interf. 22 (2021), 100845, https://doi.org/10.1016/j.surfin.2020.100845.

[26] L.-.D. Ye, F. Rouhani, H. Kaviani, Q. Miao, X.-.Q. Cai, A. Morsali, M.-.L. Hu, Effect of proton conduction on the charge storage mechanism of a MOF as a supercapacitor electrode, J. Phys. Chem. C. (2021).

[27] X. Chen, R. Tong, Z. Shi, B. Yang, H. Liu, S. Ding, X. Wang, Q. Lei, J. Wu, W. Fang, MOF nanoparticles with encapsulated autophagy inhibitor in controlled drug delivery system for antitumor, ACS Appl. Mater. Interfaces. 10 (2018) 2328–2337.

[28] E. Adatoz, A.K. Avci, S. Keskin, Opportunities and challenges of MOF-based membranes in gas separations, Sep. Purif. Technol. 152 (2015) 207–237.

[29] B. Li, Q. Guo, M. Shen, W. Li, Q. Gao, Controllable synthesis induced through cationic surfactant with two long hydrophobic chains from individual carbon spheres to 3D carbon frameworks for high performance supercapacitors, Microporous Mesoporous Mater 326 (2021), 111379, https://doi.org/10.1016/j.micromeso.2021.111379.

[30] Y. He, X. Zhang, J. Wang, Y. Sui, J. Qi, Z. Chen, P. Zhang, C. Chen, W. Liu, Constructing Co (OH) F Nanorods@ NiCo-LDH nanocages derived from ZIF-67 for high-performance supercapacitors, Adv. Mater. Interfaces. 8 (2021), 2100642.

[31] G. Nagaraju, S.C. Sekhar, B. Ramulu, S.K. Hussain, D. Narsimulu, J.S. Yu, Ternary MOF-based redox active sites enabled 3D-on-2D nanoarchitectured battery-type electrodes for high-energy-density supercapatteries, Nano-Micro Lett 13 (2021) 1–18.

[32] F. Xiao, H. Wang, T. Yao, X. Zhao, X. Yang, D.Y.W. Yu, A.L. Rogach, MOF-Derived CoS2/N-doped carbon composite to induce short-chain sulfur molecule generation for enhanced sodium–sulfur battery performance, ACS Appl. Mater. Interfaces. 13 (2021) 18010–18020.

[33] P. Sun, J. Zhang, J. Huang, L. Wang, P. Wang, C. Cai, M. Lu, Z. Yao, Y. Yang, Bimetallic MOF-derived (CuCo) Se nanoparticles embedded in nitrogen-doped carbon framework with boosted electrochemical performance for hybrid supercapacitor, Mater. Res. Bull. 137 (2021), 111196.

[34] A.P. Cohn, W.R. Erwin, K. Share, L. Oakes, A.S. Westover, R.E. Carter, R. Bardhan, C.L. Pint, All silicon electrode photocapacitor for integrated energy storage and conversion, Nano Lett 15 (2015) 2727–2731.

[35] N. Rachedi, T. Hadjersi, F. Moulai, N. Dokhane, Diamond-like carbon-coated silicon nanowires as a supercapacitor electrode in an aqueous LiClO 4 electrolyte, Silicon (2021) 1–11.

[36] Q. Zhou, M. Bao, X. Ni, A novel surface modification of silicon nanowires by polydopamine to prepare SiNWs/NC@ NiO electrode for high-performance supercapacitor, Surf. Coatings Technol. 406 (2021), 126660.

[37] Z. Wu, X. Zhang, X. Jin, T. Li, J. Ge, Z. Li, A review on cutting edge technologies of silicon-based supercapacitors, J. Nanomater. (2021) 2021.

[38] F. Lu, M. Qiu, X. Qi, L. Yang, J. Yin, G. Hao, X. Feng, J. Li, J. Zhong, Electrochemical properties of high-power supercapacitors using ordered NiO coated Si nanowire array electrodes, Appl. Phys. A. 104 (2011) 545–550.

[39] B. Wei, H. Liang, Z. Qi, D. Zhang, H. Shen, W. Hu, Z. Wang, Construction of 3D Si@ Ti@ TiN thin film arrays for aqueous symmetric supercapacitors, Chem. Commun. 55 (2019) 1402–1405.

[40] A.F.M. EL-Mahdy, T.C. Yu, S.-.W. Kuo, Synthesis of multiple heteroatom–doped mesoporous carbon/silica composites for supercapacitors, Chem. Eng. J. 414 (2021), 128796.

[41] W.-.C. Fang, O. Chyan, C.-.L. Sun, C.-.T. Wu, C.-.P. Chen, K.-.H. Chen, L.-.C. Chen, J.-.H. Huang, Arrayed CNx NT–RuO2 nanocomposites directly grown on Ti-buffered Si substrate for supercapacitor applications, Electrochem. Commun. 9 (2007) 239–244.

[42] C.K. Chan, H. Peng, G. Liu, K. McIlwrath, X.F. Zhang, R.A. Huggins, Y. Cui, High-performance lithium battery anodes using silicon nanowires, Nat. Nanotechnol. 3 (2008) 31–35.

[43] U. Kasavajjula, C. Wang, A.J. Appleby, Nano-and bulk-silicon-based insertion anodes for lithium-ion secondary cells, J. Power Sources. 163 (2007) 1003–1039.

[44] X. Su, Q. Wu, J. Li, X. Xiao, A. Lott, W. Lu, B.W. Sheldon, J. Wu, Silicon-based nanomaterials for lithium-ion batteries: a review, Adv. Energy Mater. 4 (2014), 1300882.

[45] M. Gu, Y. Li, X. Li, S. Hu, X. Zhang, W. Xu, S. Thevuthasan, D.R. Baer, J.-.G. Zhang, J. Liu, In situ TEM study of lithiation behavior of silicon nanoparticles attached to and embedded in a carbon matrix, ACS Nano 6 (2012) 8439–8447.

[46] L.A. Riley, A.S. Cavanagh, S.M. George, Y.S. Jung, Y. Yan, S. Lee, A.C. Dillon, Conformal surface coatings to enable high volume expansion li-ion anode materials, ChemPhysChem 11 (2010) 2124–2130.

[47] P. Pazhamalai, K. Krishnamoorthy, S. Sahoo, V.K. Mariappan, S.-.J. Kim, Carbothermal conversion of siloxene sheets into silicon-oxy-carbide lamellae for high-performance supercapacitors, Chem. Eng. J. 387 (2020), 123886.

[48] F.B. Ajdari, E. Kowsari, H.R. Nadri, M. Maghsoodi, A. Ehsani, H. Mahmoudi, S. K. Eshkalak, A. Chinnappan, W. Jayathilak, S. Ramakrishna, Electrochemical performance of Silsesquioxane-GO loaded with alkoxy substituted ammonium-based ionic liquid and POAP for supercapacitor, Electrochim. Acta. (2020), 136663.

[49] G.J.H. Lim, X. Liu, C. Guan, J. Wang, Co/Zn bimetallic oxides derived from metal organic frameworks for high performance electrochemical energy storage, Electrochim. Acta. 291 (2018) 177–187.

[50] X. Zhang, J. Wang, X. Ji, Y. Sui, F. Wei, J. Qi, Q. Meng, Y. Ren, Y. He, Nickel/cobalt bimetallic metal-organic frameworks ultrathin nanosheets with enhanced performance for supercapacitors, J. Alloys Compd. 825 (2020), 154069.

[51] S.H. Kazemi, B. Hosseinzadeh, H. Kazemi, M.A. Kiani, S. Hajati, Facile synthesis of mixed metal–organic frameworks: electrode materials for supercapacitors with excellent areal capacitance and operational stability, ACS Appl. Mater. Interfaces. 10 (2018) 23063–23073, https://doi.org/10.1021/acsami.8b04502.

[52] Y. Zhou, X. Li, J. Li, S. Yin, D. Shen, C. Li, P. Huo, H. Wang, Y. Yan, S. Yuan, MOF-derived Co3O4-C/Ni2P2O7 electrode material for high performance supercapacitors, Chem. Eng. J. 378 (2019), 122242.

[53] X. Zhang, J. Wang, Y. Sui, F. Wei, J. Qi, Q. Meng, Y. He, D. Zhuang, Hierarchical nickel–cobalt phosphide/phosphate/carbon nanosheets for high-performance supercapacitors, ACS Appl. Nano Mater. 3 (2020) 11945–11954.

[54] M. Saraf, R. Rajak, S.M. Mobin, A fascinating multitasking Cu-MOF/rGO hybrid for high performance supercapacitors and highly sensitive and selective electrochemical nitrite sensors, J. Mater. Chem. A. 4 (2016) 16432–16445.

[55] K.-.Y. Zou, Y.-.C. Liu, Y.-.F. Jiang, C.-.Y. Yu, M.-.L. Yue, Z.-.X. Li, Benzoate acid-dependent lattice dimension of Co-MOFs and MOF-derived CoS2@ CNTs with tunable pore diameters for supercapacitors, Inorg. Chem. 56 (2017) 6184–6196.

[56] N. Prakash, R. Balaji, S.-.M. Chen, A.P. Steffi, E. Tamilalagan, C. Narendhar, E. Muthusankar, Investigation of template-assisted (MCM-41) mesoporous Co3O4 nanostructures and its superior supercapacitive retention, Vacuum 185 (2021), 109998.

[57] Y. Zhang, Y. Zhai, FexSnyMn1-x-yO2 deposited on MCM-41 as electrode for electrochemical supercapacitor, Electrochim. Acta. 192 (2016) 328–339, https://doi.org/10.1016/j.electacta.2016.01.175.

[58] A.C. Pradhan, B. Nanda, K.M. Parida, G.R. Rao, Fabrication of the mesoporous Fe@ MnO2NPs–MCM-41 nanocomposite: an efficient photocatalyst for rapid degradation of phenolic compounds, J. Phys. Chem. C. 119 (2015) 14145–14159.

[59] X. Feng, Z. Yan, N. Chen, Y. Zhang, X. Liu, Y. Ma, X. Yang, W. Hou, Synthesis of a graphene/polyaniline/MCM-41 nanocomposite and its application as a supercapacitor, New J. Chem. 37 (2013) 2203–2209.

[60] F.B. Ajdari, M.D. Najafi, M.I. Ostad, H. reza Naderi, M.N. Shahrak, E. Kowsari, S. Ramakrishna, A symmetric ZnO-ZIF8//Mo-ZIF8 supercapacitor and comparing with electrochemical of Pt, Au, and Cu decorated ZIF-8 electrodes, J. Mol. Liq. 333 (2021), 116007.

[61] A. Ehsani, E. Kowsari, F.B. Ajdari, R. Safari, H.M. Shiri, Sulfonated graphene oxide and its nanocomposites with electroactive conjugated polymer as effective pseudocapacitor electrode materials, J. Colloid Interface Sci. 497 (2017) 258–265.

[62] F.B. Ajdari, E. Kowsari, A. Ehsani, L. Chepyga, M. Schirowski, S. Jäger, O. Kasian, F. Hauke, T. Ameri, Melamine-functionalized graphene oxide: synthesis, characterization and considering as pseudocapacitor electrode material with intermixed POAP polymer, Appl. Surf. Sci. 459 (2018) 874–883, https://doi.org/10.1016/j.apsusc.2018.07.215.

[63] M.J. Katz, Z.J. Brown, Y.J. Colón, P.W. Siu, K.A. Scheidt, R.Q. Snurr, J.T. Hupp, O.K. Farha, A facile synthesis of UiO-66, UiO-67 and their derivatives, Chem. Commun. 49 (2013) 9449–9451.

[64] M.R. DeStefano, T. Islamoglu, S.J. Garibay, J.T. Hupp, O.K. Farha, Room-temperature synthesis of UiO-66 and thermal modulation of densities of defect sites, Chem. Mater. 29 (2017) 1357–1361.

[65] A.M. Sabzevar, M. Ghahramaninezhad, M.N. Shahrak, Enhanced biodiesel production from oleic acid using TiO2-decorated magnetic ZIF-8 nanocomposite catalyst and its utilization for used frying oil conversion to valuable product, Fuel 288 (2021), 119586.

[66] H. Ghorbani, M. Ghahramaninezhad, M.N. Shahrak, The effect of organic and ionic liquid solvents on structure crystallinity and crystallite size of ZIF-8 for CO2 uptake, J. Solid State Chem. 289 (2020), 121512.

[67] A. Helal, M. Usman, M.E. Arafat, M.M. Abdelnaby, Allyl functionalized UiO-66 metal-organic framework as a catalyst for the synthesis of cyclic carbonates by CO2 cycloaddition, J. Ind. Eng. Chem. 89 (2020) 104–110.

[68] R. Ediati, P. Elfianuar, E. Santoso, D.O. Sulistiono, M. Nadjib, Synthesis of MCM-41/ZIF-67 composite for enhanced adsorptive removal of methyl orange in aqueous solution. Mesoporous Mater. Appl., IntechOpen London, UK, 2019.

[69] R. Saeedirad, S.T. Ganjali, M. Bazmi, A. Rashidi, Effective mesoporous silica-ZIF-8 nano-adsorbents for adsorptive desulfurization of gas stream, J. Taiwan Inst. Chem. Eng. 82 (2018) 10–22.

[70] M. Pérez-Miana, J.U. Reséndiz-Ordóñez, J. Coronas, Solventless synthesis of ZIF-L and ZIF-8 with hydraulic press and high temperature, Microporous Mesoporous Mater 328 (2021), 111487, https://doi.org/10.1016/j.micromeso.2021.111487.

[71] M. Izadpanah Ostad, M. Niknam Shahrak, F. Galli, Photocatalytic carbon dioxide reduction to methanol catalyzed by ZnO, Pt, Au, and Cu nanoparticles decorated zeolitic imidazolate framework-8, J. CO2 Util. 43 (2021), 101373, https://doi.org/10.1016/j.jcou.2020.101373.

[72] H.N. Abdelhamid, UiO-66 as a catalyst for hydrogen production via the hydrolysis of sodium borohydride, Dalt. Trans. 49 (2020) 10851–10857.

[73] L. Zhu, L. Zhou, N. Huang, W. Cui, Z. Liu, K. Xiao, Z. Zhou, Efficient preparation of enantiopure D-phenylalanine through asymmetric resolution using immobilized phenylalanine ammonia-lyase from Rhodotorula glutinis JN-1 in a recirculating packed-bed reactor, PLoS ONE 9 (2014), e108586.

[74] S. Wang, J. Cui, S. Zhang, X. Xie, W. Xia, Enhancement thermal stability and CO2 adsorption property of ZIF-8 by pre-modification with polyaniline, Mater. Res. Express. 7 (2020) 25304.

[75] B. Chameh, M. Moradi, S. Hajati, F.A. Hessari, Design and construction of ZIF (8 and 67) supported Fe3O4 composite as advanced materials of high performance supercapacitor, Phys. E Low-Dimensional Syst. Nanostructures. 126 (2021), 114442.

[76] Q. Wang, J. Yan, Y. Wang, T. Wei, M. Zhang, X. Jing, Z. Fan, Three-dimensional flower-like and hierarchical porous carbon materials as high-rate performance electrodes for supercapacitors, Carbon N. Y. 67 (2014) 119–127.

[77] S. Zhong, C. Zhan, D. Cao, Zeolitic imidazolate framework-derived nitrogen-doped porous carbons as high performance supercapacitor electrode materials, Carbon N. Y. 85 (2015) 51–59, https://doi.org/10.1016/j.carbon.2014.12.064.
[78] R. Kumar, M. Singh, A. Soam, Study on electrochemical properties of Silicon micro particles as electrode for supercapacitor application, Surfaces and Interfaces (2020), 100524.
[79] L. Oakes, A. Westover, J.W. Mares, S. Chatterjee, W.R. Erwin, R. Bardhan, S. M. Weiss, C.L. Pint, Surface engineered porous Silicon for stable, high performance electrochemical supercapacitors, Sci. Rep. 3 (2013) 3020, https://doi.org/10.1038/srep03020.
[80] X. Wang, Y. Yin, X. Li, Z. You, Fabrication of a symmetric micro supercapacitor based on tubular ruthenium oxide on silicon 3D microstructures, J. Power Sources. 252 (2014) 64–72, https://doi.org/10.1016/j.jpowsour.2013.11.109.
[81] Y. He, D. Liu, H. Zhao, J. Wang, Y. Sui, J. Qi, Z. Chen, P. Zhang, C. Chen, D. Zhuang, Carbon-coated NiMn layered double hydroxides/Ni3S2 nanocomposite for high performance supercapacitors, J. Energy Storage. 41 (2021), 103003.
[82] Z. Chen, V. Augustyn, J. Wen, Y. Zhang, M. Shen, B. Dunn, Y. Lu, High-performance supercapacitors based on intertwined CNT/V2O5 nanowire nanocomposites, Adv. Mater. 23 (2011) 791–795.
[83] F.B. Ajdari, E. Kowsari, A. Ehsani, M. Schorowski, T. Ameri, New synthesized ionic liquid functionalized graphene oxide: synthesis, characterization and its nanocomposite with conjugated polymer as effective electrode materials in an energy storage device, Electrochim. Acta. 292 (2018) 789–804.
[84] F.B. Ajdari, E. Kowsari, A. Ehsani, Ternary nanocomposites of conductive polymer/functionalized GO/MOFs: synthesis, characterization and electrochemical performance as effective electrode materials in pseudocapacitors, J. Solid State Chem. 265 (2018) 155–166, https://doi.org/10.1016/j.jssc.2018.05.038.
[85] B. Liu, H. Shioyama, H. Jiang, X. Zhang, Q. Xu, Metal-organic framework (MOF) as a template for syntheses of nanoporous carbons as electrode materials for supercapacitor, Carbon N. Y. 48 (2010) 456–463, https://doi.org/10.1016/j.carbon.2009.09.061.
[86] A. Laheäär, S. Delpeux-Ouldriane, E. Lust, F. Béguin, Ammonia treatment of activated carbon powders for supercapacitor electrode application, J. Electrochem. Soc. 161 (2014) A568.
[87] X. Hong, K.S. Hui, Z. Zeng, K.N. Hui, L. Zhang, M. Mo, M. Li, Hierarchical nitrogen-doped porous carbon with high surface area derived from endothelium corneum gigeriae galli for high-performance supercapacitor, Electrochim. Acta. 130 (2014) 464–469.
[88] W. Li, X. Sun, Y. Yu, Ge- Si-, Sn-based anode materials for lithium-ion batteries: from structure design to electrochemical performance, Small Meth. 1 (2017), 1600037.
[89] Q. Wei, Y.-.M. Chen, X.-.J. Hong, C.-.L. Song, Y. Yang, L.-.P. Si, M. Zhang, Y.-.P. Cai, Saclike-silicon nanoparticles anchored in ZIF-8 derived spongy matrix as high-performance anode for lithium-ion batteries, J. Colloid Interface Sci. 565 (2020) 315–325, https://doi.org/10.1016/j.jcis.2020.01.050.
[90] Q. Li, Y. Wang, X. Gao, H. Li, Q. Tan, Z. Zhong, F. Su, Enhancement of ZIF-8 derived N-doped carbon/silicon composites for anode in lithium ions batteries, J. Alloys Compd. 872 (2021), 159712, https://doi.org/10.1016/j.jallcom.2021.159712.
[91] A. Ehsani, E. Kowsari, F. Boorboor Ajdari, R. Safari, H.Mohammad Shiri, Influence of newly synthesized geminal dicationic ionic liquid on electrochemical and pseudocapacitance performance of conductive polymer electroactive film, J. Colloid Interface Sci. 505 (2017) 1158–1164, https://doi.org/10.1016/j.jcis.2017.07.001.
[92] U. Samukaite-Bubniene, A. Valiūnienė, V. Bucinskas, P. Genys, V. Ratautaite, A. Ramanaviciene, E. Aksun, A. Tereshchenko, B. Zeybek, A. Ramanavicius, Towards supercapacitors: cyclic voltammetry and fast fourier transform electrochemical impedance spectroscopy based evaluation of polypyrrole electrochemically deposited on the pencil graphite electrode, Colloids Surfaces A Physicochem. Eng. Asp. 610 (2021), 125750, https://doi.org/10.1016/j.colsurfa.2020.125750.
[93] M.M. Baig, E. Pervaiz, M. Azad, Z. Jahan, M.B. Khan Niazi, S.M. Baig, NiFe2O4/SiO2 nanostructures as a potential electrode material for high rated supercapacitors, Ceram. Int. 47 (2021) 12557–12566, https://doi.org/10.1016/j.ceramint.2021.01.113.
[94] M.U. Tahir, H. Arshad, H. Zhang, Z. Hou, J. Wang, C. Yang, X. Su, Room temperature and aqueous synthesis of bimetallic ZIF derived CoNi layered double hydroxides and their applications in asymmetric supercapacitors, J. Colloid Interface Sci. 579 (2020) 195–204, https://doi.org/10.1016/j.jcis.2020.06.050.
[95] D. Prakash, S. Manivannan, N, B co-doped and crumpled graphene oxide pseudocapacitive electrode for high energy supercapacitor, Surfaces and Interfaces 23 (2021), 101025, https://doi.org/10.1016/j.surfin.2021.101025.
[96] S.K. Ramasahayam, U.B. Nasini, A.U. Shaikh, T. Viswanathan, Novel tannin-based Si, P co-doped carbon for supercapacitor applications, J. Power Sources. 275 (2015) 835–844, https://doi.org/10.1016/j.jpowsour.2014.11.020.
[97] W. Zhang, N. Lin, D. Liu, J. Xu, J. Sha, J. Yin, X. Tan, H. Yang, H. Lu, H. Lin, Direct carbonization of rice husk to prepare porous carbon for supercapacitor applications, Energy 128 (2017) 618–625.
[98] D. Zhang, J. Zhang, M. Pan, Y. Wang, T. Sun, Necklace-like C-ZIF-8@MWCNTs fabricated by electrochemical deposition towards enhanced supercapacitor, J. Alloys Compd. 853 (2021), 157368, https://doi.org/10.1016/j.jallcom.2020.157368.
[99] H. Lee, I.-.S. Park, H.-.J. Bang, Y.-.K. Park, E.-.B. Cho, B.-.J. Kim, S.-.C. Jung, Preparation of silicon oxide–carbon composite from benzene and trimethoxyphenylsilane by a liquid phase plasma method for supercapacitor applications, Appl. Surf. Sci. 481 (2019) 625–631.
[100] I. Oh, M. Kim, J. Kim, Carbon-coated Si/MnO2 nanoneedle composites with optimum carbon layer activation for supercapacitor applications, Chem. Eng. J. 273 (2015) 82–91, https://doi.org/10.1016/j.cej.2015.03.078.
[101] D. Antiohos, G. Folkes, P. Sherrell, S. Ashraf, G.G. Wallace, P. Aitchison, A. T. Harris, J. Chen, A.I. Minett, Compositional effects of PEDOT-PSS/single walled carbon nanotube films on supercapacitor device performance, J. Mater. Chem. 21 (2011) 15987–15994.
[102] A. Hosseinian, A. Amjad, R. Hosseinzadeh-Khanmiri, E. Ghorbani-Kalhor, M. Babazadeh, E. Vessally, Nanocomposite of ZIF-67 metal–organic framework with reduced graphene oxide nanosheets for high-performance supercapacitor applications, J. Mater. Sci. Mater. Electron. 28 (2017) 18040–18048, https://doi.org/10.1007/s10854-017-7747-z.
[103] C. Zhang, J. Tian, W. Rao, B. Guo, L. Fan, W. Xu, J. Xu, Polypyrrole@metal-organic framework (UIO-66)@cotton fabric electrodes for flexible supercapacitors, Cellulose 26 (2019) 3387–3399, https://doi.org/10.1007/s10570-019-02321-3.
[104] X. Li, C. Hao, B. Tang, Y. Wang, M. Liu, Y. Wang, Y. Zhu, C. Lu, Z. Tang, Supercapacitor electrode materials with hierarchically structured pores from carbonization of MWCNTs and ZIF-8 composites, Nanoscale 9 (2017) 2178–2187, https://doi.org/10.1039/C6NR08987A.
[105] L. Shao, Q. Wang, Z. Ma, Z. Ji, X. Wang, D. Song, Y. Liu, N. Wang, A high-capacitance flexible solid-state supercapacitor based on polyaniline and metal-organic framework (UiO-66) composites, J. Power Sources. 379 (2018) 350–361, https://doi.org/10.1016/j.jpowsour.2018.01.028.
[106] Y. Wang, B. Chen, Y. Zhang, L. Fu, Y. Zhu, L. Zhang, Y. Wu, ZIF-8@MWCNT-derived carbon composite as electrode of high performance for supercapacitor, Electrochim. Acta. 213 (2016) 260–269, https://doi.org/10.1016/j.electacta.2016.07.019.